Electrohydrodynamics of a viscous drop with inertia

H. Nganguia
Department of Mathematical Sciences, New Jersey Institute of Technology, Newark, New Jersey, USA and Akili Software & Analytics Consulting, Raleigh, North Carolina, USA

Y.-N. Young*
Department of Mathematical Sciences, New Jersey Institute of Technology, Newark, New Jersey, USA

A. T. Layton
Department of Mathematics, Duke University, Durham, North Carolina, USA

M.-C. Lai
Department of Applied Mathematics, National Chiao-Tung University, Taiwan

W.-F. Hu
Department of Applied Mathematics, National Chung Hsing University, Taiwan

(Received 23 December 2015; revised manuscript received 5 May 2016; published 23 May 2016)

Most of the existing numerical and theoretical investigations on the electrohydrodynamics of a viscous drop have focused on the creeping Stokes flow regime, where nonlinear inertia effects are neglected. In this work we study the inertia effects on the electrodeformation of a viscous drop under a DC electric field using a novel second-order immersed interface method. The inertia effects are quantified by the Ohnesorge number Oh, and the electric field is characterized by an electric capillary number Ca_E. Below the critical Ca_E, small to moderate electric field strength gives rise to steady equilibrium drop shapes. We found that, at a fixed Ca_E, inertia effects induce larger deformation for an oblate drop than a prolate drop, consistent with previous results in the literature. Moreover, our simulations results indicate that inertia effects on the equilibrium drop deformation are dictated by the direction of normal electric stress on the drop interface: Larger drop deformation is found when the normal electric stress points outward, and smaller drop deformation is found otherwise. To our knowledge, such inertia effects on the equilibrium drop deformation has not been reported in the literature. Above the critical Ca_E, no steady equilibrium drop deformation can be found, and often the drop breaks up into a number of daughter droplets. In particular, our Navier-Stokes simulations show that, for the parameters we use, (1) daughter droplets are larger in the presence of inertia, (2) the drop deformation evolves more rapidly compared to creeping flow, and (3) complex distribution of electric stresses for drops with inertia effects. Our results suggest that normal electric pressure may be a useful tool in predicting drop pinch-off in oblate deformations.

DOI: 10.1103/PhysRevE.93.053114

I. INTRODUCTION

The wide application and relevance of the electrohydrodynamics of a viscous drop in a uniform electric field have attracted extensive theoretical studies [1–5], numerical investigations [6–8], and physical experiments [9–14]. For a leaky dielectric drop in a leaky dielectric fluid, the deformation depends on the ratios of conductivities and permittivities between the drop and the surrounding fluid. The drop can deform into a prolate or oblate spheroid, and the degree of deformation depends on the strength of the electric field. Furthermore, the electrohydrodynamics of a surfactant-laden viscous drop exhibits rich dependence on surfactant coverage and elasticity [15].

In a comparative numerical study of drop electrohydrodynamics that contrasted results in creeping flow with those with inertia, Feng and Scott [16] showed that Navier-Stokes flow resulted in larger drop deformation. Their results suggest a positive correlation between drop size and Reynolds number that lead to a reduction in the critical threshold for equilibrium deformation. When the electric field strength (characterized by the electric capillary number Ca_E) is increased beyond a critical threshold, steady equilibrium deformation no longer exists and the drop exhibits a wide variety of dynamics. Experimental studies [9–14] have illustrated the electrohydrodynamics of a viscous drop above critical electric capillary values. Two modes of breakup have been observed. In one mode, the drop forms pointed ends known as Taylor cones along the direction of the field, before releasing droplets in a jet-like manner. In the other mode, the drop undergoes pinch-off, in which the original drop splits in half at its center with bulbous ends. Numerical studies have been able to capture some of these dynamics [17,18].

In a comprehensive numerical study of drop electrohydrodynamics above critical electric capillary number, Lac and Homsy [7] showed that in addition to breaking up as described above, the drop can also deform indefinitely, taking increasingly more slender, elongated shapes. The authors employ the widely used boundary integral method, based on the working assumption of creeping flow. Other groups

*yyoung@njit.edu

resolved the flow field using the full incompressible Navier-Stokes equations, also capturing breakup [8,19,20]. However, they did not explore the effects of inertia in a systematic manner. In addition, their numerical approaches were either too computationally expensive [8] or only first-order accurate [19].

Lanauze *et al.* [21] developed an analytical model that described the effect of inertia (captured by the Ohnesorge number) on drop deformation. They show the magnitude of the Ohnesorge number determines the presence or absence of an overshoot in the transient deformation profile; i.e., the magnitude of the deformation number exceeds its steady-state value. Moreover, the model is only valid for small deviations from the drop's initially spherical shape (in the regime of small electric capillary number). Previous computational studies have investigated the inertia effects on drop electrohydrodynamics [8]. A systematic numerical study of inertia effects on steady equilibrium drop shape is provided in Feng and Scott [16], where the equilibrium drop shapes under an electric field are obtained by solving the steady Navier-Stokes equations. In this paper we conduct a systematic numerical investigation of the inertia effects on both the steady equilibrium drop shape and the electrohydrodynamic of a leaky dielectric drop suspended in a leaky dielectric fluid, subject to a uniform DC electric field. In addition we also focus on the distribution of both electric and viscous stresses on the drop interface. Moreover, our numerical simulations extend to drop dynamics at the onset of drop pinch-off under a strong electric field. The results are presented to illustrate the effects of both electric capillary number, Ca_E, and inertia (characterized by the Ohnesorge number, Oh) on the deformation and electric stresses acting on the drop.

The paper is organized as follows. In Sec. II, we describe the physical problem and introduce the equations governing the electrohydrodynamics of a viscous drop. We then describe the numerical methods in Sec. III and discuss key implementation details of the immersed interface method (IIM). In Sec. IV we present our findings, and finally we discuss our results in Sec. V.

II. PROBLEM FORMULATION

A schematic diagram of the problem formulation is shown in Fig. 1: we consider an initially spherical viscous drop under an electric field $\boldsymbol{E}_0$, whose direction is parallel to the axis of symmetry. The interface Γ separates the exterior fluid

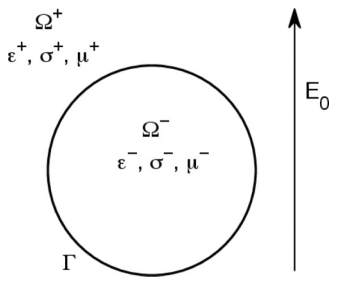

FIG. 1. Sketch of the problem: A leaky dielectric viscous drop (in domain Ω^-) immersed in another leaky dielectric fluid (in domain Ω^+), with an external electric field E_0 in the z direction. Subscript "+" and "−" denote the exterior and interior fluids, respectively.

(superscript "+" for the exterior domain Ω^+) from the interior fluid (superscript "−" for the interior domain Ω^-). Within each fluid, the velocity field is described by the incompressible Navier-Stokes equation

$$\rho^j\left(\frac{\partial \boldsymbol{u}^j}{\partial t}+\boldsymbol{u}^j\cdot\nabla\boldsymbol{u}^j\right)=-\nabla p^j+\mu^j\nabla^2\boldsymbol{u}^j, \tag{1}$$

$$\nabla\cdot\boldsymbol{u}^j=0, \tag{2}$$

where $j=$"+" for the exterior fluid and $j=$"−" for the interior fluid. Here, we assume matching fluid densities and viscosities: $\rho^+=\rho^-$ and $\mu^+=\mu^-$. In the bulk the electric permittivity ε^j and conductivity σ^j may be different between the exterior ("+") and interior ("−") of the drop. The ratios of permittivities and conductivities are defined as

$$\varepsilon_r=\frac{\varepsilon^-}{\varepsilon^+},\qquad \sigma_r=\frac{\sigma^-}{\sigma^+}. \tag{3}$$

The drop interface Γ is given in parametric form $\boldsymbol{X}(s,t)=(R(s,t),Z(s,t))$ with $s=0$ at the equator in the first quadrant. Under an external electric field, bulk charges neutralize instantaneously in the leaky dielectric framework [2], and consequently the electric potential ϕ satisfies the Laplace equation,

$$\nabla\cdot(\varepsilon\nabla\phi)=0, \tag{4}$$

with boundary conditions at the interface,

$$[\![\phi]\!]=0,\qquad [\![\sigma\nabla\phi\cdot\boldsymbol{n}]\!]=\frac{dq_s}{dt}, \tag{5}$$

at the drop interface. $\boldsymbol{n}$ is the unit outward normal, $q_s=[\![\varepsilon\nabla\phi\cdot\boldsymbol{n}]\!]$ represents the surface charge density, and $[\![\cdot]\!]$ denotes the jump between outside and inside quantities. In general, the charging time $t_c\equiv\varepsilon^j/\sigma^j$ is much faster than the time scale $t_{\mathrm{EHD}}=\mu^j/\varepsilon^jE_0^2$ of the electrohydrodyanimc flow: $t_c\ll t_{\mathrm{EHD}}$. Therefore, the charge relaxation term on the righthand side of Eq. (5) can be ignored [16,22], and the jump condition on the normal electric field reduces to $[\![\sigma\nabla\phi\cdot\boldsymbol{n}]\!]=0$. In the far field, the electric potential satisfies $\nabla\phi^+=-\boldsymbol{E}_0\hat{\boldsymbol{z}}$. The electric force $\boldsymbol{F}_E$ is related to the Maxwell stress $\mathbf{M}$ as $\boldsymbol{F}_E=\nabla\cdot\mathbf{M}$, with $\mathbf{M}$ computed from the electric field $\boldsymbol{E}$ as

$$\mathbf{M}=\varepsilon\left(\boldsymbol{E}\boldsymbol{E}-\tfrac{1}{2}E^2\mathbf{I}\right), \tag{6}$$

where $\mathbf{I}$ is the identity tensor. In the leaky dielectric formulation, the electric force is important only when there is a gradient or jump in the electrical conductivity σ and/or permittivity ε. As these electrical properties are assumed to be piecewise constant with a possible jump across the drop interface in our formulation (see Fig. 1), the electric force $\boldsymbol{F}_E$ can be treated as an interfacial force given by the jump in Maxwell stress in the normal direction, as done in the boundary integral method [23].

At the drop interface, the stress balance gives

$$(-p^++p^-)\mathbf{n}+[\![\mathbf{T}^{\mathrm{hd}}]\!]\cdot\mathbf{n}+\boldsymbol{f}=0, \tag{7}$$

where $(\mathbf{T}^{\mathrm{hd}})_{ij}\equiv\mu(\partial_iu_j+\partial_ju_i)$ is the ij-th component of the viscous stress tensor. The traction $\boldsymbol{f}$ consists of the surface

tension [24,25] and electric force, and is given by

$$\boldsymbol{f} = \boldsymbol{f}_\gamma + \boldsymbol{f}_E = \gamma\left(\frac{R_s Z_{ss} - R_{ss} Z_s}{|\boldsymbol{X}_s|^3} + \frac{Z_s}{R}\right)\boldsymbol{n} + [\![\mathbf{M}\cdot\boldsymbol{n}]\!], \tag{8}$$

where γ is the drop surface tension, $|\boldsymbol{X}_s| = \sqrt{R_s^2 + Z_s^2}$, and the subscript "$s$" denotes partial derivatives with respect to s.

III. NUMERICAL METHODS

Prior to solving the governing equations, the system is nondimensionalized using the following scaling: $\mathbf{x} = r_0\mathbf{x}^*$, $p = \frac{\gamma}{r_0}p^*$, $\boldsymbol{u} = \sqrt{\frac{\gamma}{\rho r_0}}\boldsymbol{u}^*$, and $t = \sqrt{\frac{\rho r_0^3}{\gamma}}T^*$. Here, r_0 is the initial radius of the drop, and ρ is the fluid density. The dimensionless governing equations become (after dropping the *)

$$\frac{\partial \boldsymbol{u}}{\partial T} + \boldsymbol{u}\cdot\nabla\boldsymbol{u} = -\nabla p + \mathrm{Oh}\Delta\boldsymbol{u} + \int_0^{2\pi} (\boldsymbol{f}_\gamma + \mathrm{Ca}_E\boldsymbol{f}_E)\delta^2(\boldsymbol{x} - \boldsymbol{X}(s,t))ds, \tag{9}$$

$$\nabla\cdot\boldsymbol{u} = 0, \tag{10}$$

$$\nabla\cdot(\varepsilon\nabla\phi) = 0, \quad [\![\phi]\!] = 0, \quad [\![\sigma\phi_n]\!] = 0, \tag{11}$$

$$\boldsymbol{E} = -\nabla\phi, \quad \mathbf{M} = \varepsilon\left(\boldsymbol{E}\boldsymbol{E} - \frac{1}{2}E^2\mathbf{I}\right),$$

$$\boldsymbol{f}_E = [\![\mathbf{M}]\!]\cdot\boldsymbol{n} \text{ and } \boldsymbol{f}_\gamma = \left(\frac{R_s Z_{ss} - R_{ss} Z_s}{|\boldsymbol{X}_s|^3} + \frac{Z_s}{R}\right)\boldsymbol{n}. \tag{12}$$

In addition to the ratios of permittivities and conductivities, ε_r, σ_r, the other dimensionless parameters of the problem are the Ohnesorge number and the electric capillary number:

$$\mathrm{Oh} = \mu/\sqrt{\rho\gamma r_0}, \qquad \mathrm{Ca}_E = \varepsilon^+ E_0^2 r_0/\gamma. \tag{13}$$

The Ohnesorge number represents the ratio of viscous force to inertial and surface tension, and the electric capillary number reflects the strength of the electric field. Moreover, the Ohnesorge number is inversely proportional to the Reynolds number, Re: $\mathrm{Oh} = \sqrt{\frac{\mathrm{Ca}}{\mathrm{Re}}}$, where Ca is the capillary number.

We consider Eqs. (9)–(12) with axial symmetry in cylindrical coordinates (r,z) and solve them over the $r \geqslant 0$ half-plane (due to axisymmetry). In a previous study [26], we used the immersed interface method to simulate the axisymmetric electrohydrodynamic of a viscous drop. We also conducted preliminary simulations of extreme drop deformation toward breakup and obtained good agreement with results from previous work [7]. Key components of the model [26] are described below.

The augmented immersed interface method from Hu *et al.* [27] is used to solve for the electric potential [Eq. (11)] and compute the electric force on the drop interface. The solutions in the interior and exterior of the drop are treated independently, and both solutions are coupled at the drop interface by introducing a new interfacial condition, called the *augmented variable*. As such, a fast solver can be used in the exterior and interior domains while the solution on the drop interface is obtained using GMRES.

For the flow field, we follow the velocity decomposition approach [28,29] to solve Eq. (9). In this approach, velocity and pressure are split into a Stokes component (subscript s) and a continuous component (subscript c) as

$$\boldsymbol{u} = \boldsymbol{u}_s + \boldsymbol{u}_c, \qquad p = p_s + p_c. \tag{14}$$

$(\boldsymbol{u}_s, p_s)$ satisfies the incompressible Stokes equations, and is computed using the schemes described in Ref. [26]. Once the Stokes solution is known, we substitute Eq. (14) into Eq. (9) to obtain the equations governing the continuous field:

$$\frac{\partial \boldsymbol{u}_c}{\partial t} + \boldsymbol{u}\cdot\nabla\boldsymbol{u}_c = -\nabla p_c + \mu\Delta\boldsymbol{u}_c + \boldsymbol{F}_b, \tag{15}$$

$$\nabla\cdot\boldsymbol{u}_c = 0, \tag{16}$$

where the body force is

$$\boldsymbol{F}_b = -\frac{\partial \boldsymbol{u}_s}{\partial t} - \boldsymbol{u}\cdot\nabla\boldsymbol{u}_s. \tag{17}$$

The equations are then solved by projection method, with time discretized using a second-order Adams-Bashforth scheme.

IV. RESULTS

A. Convergence Results

We first perform a convergence analysis to determine the appropriate spatial and temporal discretizations. In our simulations, the time step, $\triangle t$, is proportional to the spatial discretization, h, and is given by $\triangle t = h/75$, where $h = L/N$. The computational domain size L is set to 7.5. To validate convergence, we compare our simulations with the base state reported by Supeene *et al.* [8], where $E = 1$ MV/m (electric capillary number, $\mathrm{Ca}_E = 0.009$). For the simulations, the densities of the drop and ambient fluid are considered to be the same, $\rho = \rho^+ = \rho^- = 1000$ kg/m^3. We consider matching viscosities between the two fluids $\mu = \mu^+ = \mu^- = 0.001$ Pa · s, and the surface tension $\gamma = 0.03$ N/m. The ratio of electrical properties are $\sigma_r = 1$, $\varepsilon_r = 80/3$. With these values of electrical property ratios, the drop deforms into an oblate shape. For a drop radius, $r_0 = 1$ μm, we obtain the Ohnesorge number $\mathrm{Oh} = 0.1836$ from Eq. (13). Figure 2 shows the ratio of drop deformation, D, to the deformation

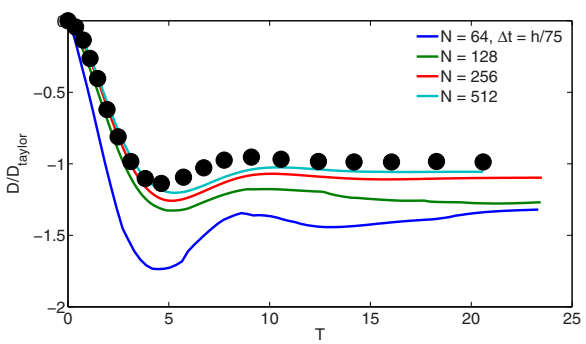

FIG. 2. Convergence results for the proposed IIM. (●) are simulations using the FEM implementation for the base state from Supeene *et al.* [8]. The ratio is shown as negative values, with the (−) sign denoting oblate deformation.

predicted by the Taylor's approximation as a function of dimensionless time. The deformation number

$$D = \frac{a-b}{a+b}, \tag{18}$$

where a (b) is the drop size in the direction parallel (orthogonal) to the electric field. Based on these convergence results, we fixed $N = 512$ in all the Navier-Stokes simulations presented in this paper, unless otherwise noted.

B. Equilibrium deformation

In the leaky dielectric formulation, equilibrium drop deformations are achieved when the electric force (Maxwell stress) is balanced by the surface tension force on the drop interface. At steady state a circulatory flow forms inside the drop: With a uniform electric field from south to north poles, the circulation is from the equator to the pole in a prolate drop, and from the pole to the equator in an oblate drop. Equilibrium deformation of a drop subject to a uniform DC electric field and inertia has been previously reported [16]. Larger equilibrium deformation is found in the presence of inertia, compared to drop deformation in creeping flow. Moreover, the critical electric capillary number (corresponding to the electric field strength beyond which equilibrium deformation ceases to exist) is reduced by the nonlinear inertia effects. To investigate the inertia effects on the equilibrium drop shape, parameters from our previous work [26] are used for both the prolate and oblate drops. Figure 3 shows the drop deformation number D as a function of electric capillary number Ca_E. The ratios of electric properties are $\sigma_r = 10$, $\varepsilon_r = 0.1$ for the prolate drop ($D > 0$), and $\sigma_r = 0.1$, $\varepsilon_r = 2$ for the oblate drop ($D < 0$) [7].

For $\mathrm{Ca}_E \leqslant 0.15$, there is little difference between our Navier-Stokes simulation results, boundary integral method (BIM) simulation results [7], and predictions from our spheroidal model [15]. This suggests that inertia effects are not important at small Ca_E, and the deformation is well approximated by the creeping flow theory. For $\mathrm{Ca}_E > 0.15$ we observe significant inertia effects on equilibrium oblate deformations ($D < 0$), which are larger than the corresponding drop deformations in creeping flow. Such inertia effects, however, are not observed for prolate deformations ($D > 0$), for which the creeping flow theory remains valid over a larger range of capillary numbers, up to $\mathrm{Ca}_E \approx 0.32$.

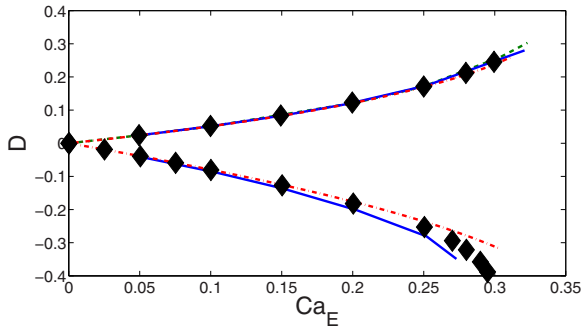

FIG. 3. Drop deformation D as a function of electric capillary number Ca_E for prolate ($D > 0$) and oblate ($D < 0$) drops. For the prolate drop conductivity and permittivity ratios are $\sigma_r = 10$, $\varepsilon_r = 0.1$. For the oblate drop $\sigma_r = 0.1$, $\varepsilon_r = 2$. The comparisons show results from the IIM and BIM [7] ($\Diamond$) simulations, as well as the prediction from the spheroidal model [5,15] (dash-dotted). The Ohnesorge numbers are Oh = 0.459 (solid) and Oh = 0.1836 (dashed).

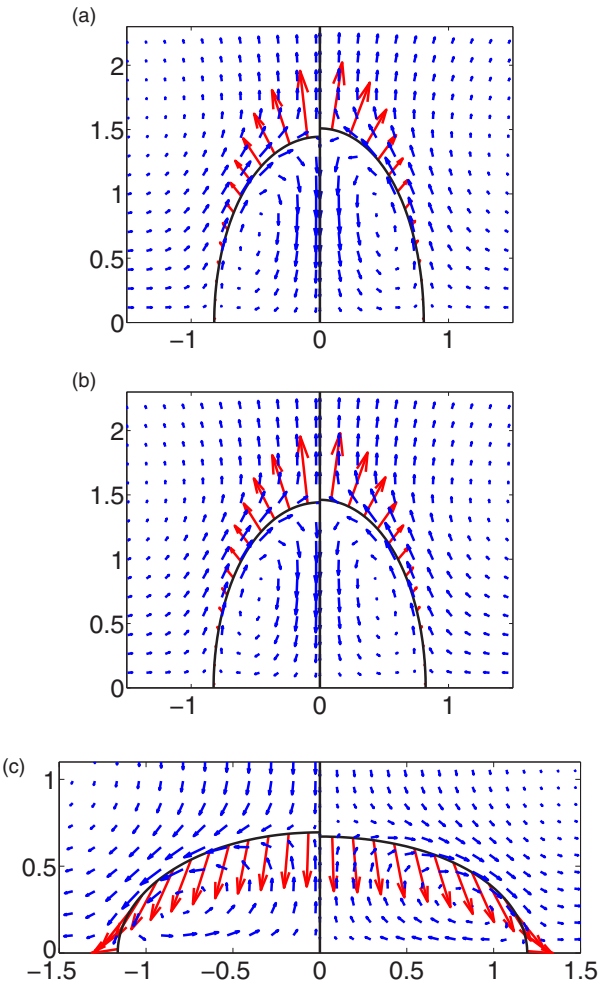

FIG. 4. Comparison between creeping flow (left panel) and Navier-Stokes flow (right panel) for steady-state shape of upper half of drop. The red arrows represent the electric force acting on the drop interface. (a, b) Prolate drop: $\sigma_r = 10$, $\varepsilon_r = 0.1$. The Ohnesorge and electric capillary numbers are (a) Oh = 0.1836,$\mathrm{Ca}_E = 0.32$, and (b) Oh = 0.459,$\mathrm{Ca}_E = 0.32$. (c) Oblate drop: $\sigma_r = 0.1$, $\varepsilon_r = 2$. The Ohnesorge and electric capillary numbers are Oh = 0.459,$\mathrm{Ca}_E = 0.253$.

Figure 4(a) shows comparison between prolate deformations in creeping flow (left panel) and Navier-Stokes flow (right panel) for Oh = 0.1836. As shown in Fig. 5, the difference in shape between the two cases is due to stronger positive electric stress at the pole in the presence of inertia. In Fig. 4(b) (prolate with $\mathrm{Ca}_E = 0.32$ and Oh = 0.459), inertia gives rise to a slightly larger equilibrium deformation, while the opposite is observed in Fig. 4(c) (oblate with $\mathrm{Ca}_E = 0.253$ and Oh = 0.459).

Figure 5 shows the normal and tangential electric stresses for Fig. 4(a) (prolate drop with $D > 0$), as a function of arc length s (where $s = 0$ at the equator). While there is little

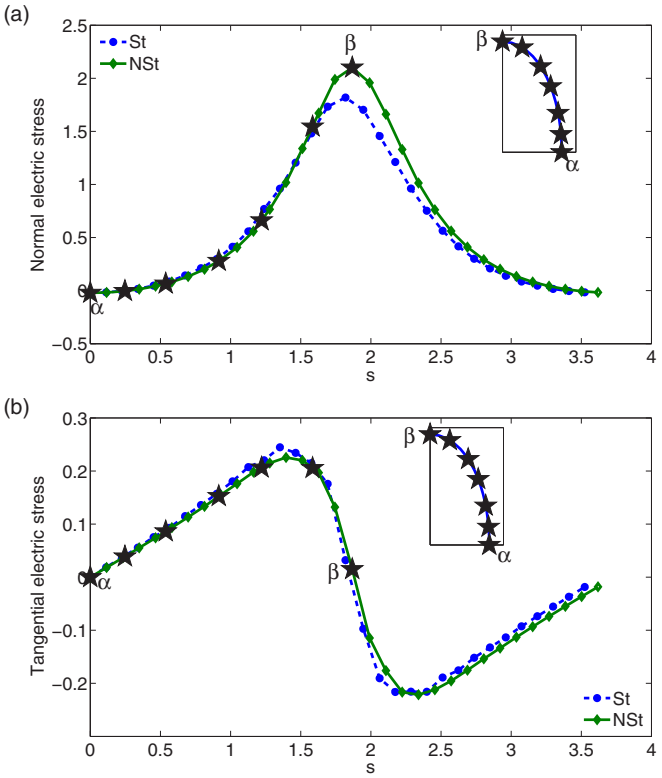

FIG. 5. Normal (a) and tangential (b) electric stresses for Fig. 4(a). (prolate drop). $Ca_E = 0.32$, $Oh = 0.1836$ (solid) and $Oh \to \infty$ (dashed, limit of creeping flow). In the legend, *St* denotes Stokes, and *NSt* denotes Navier-Stokes.

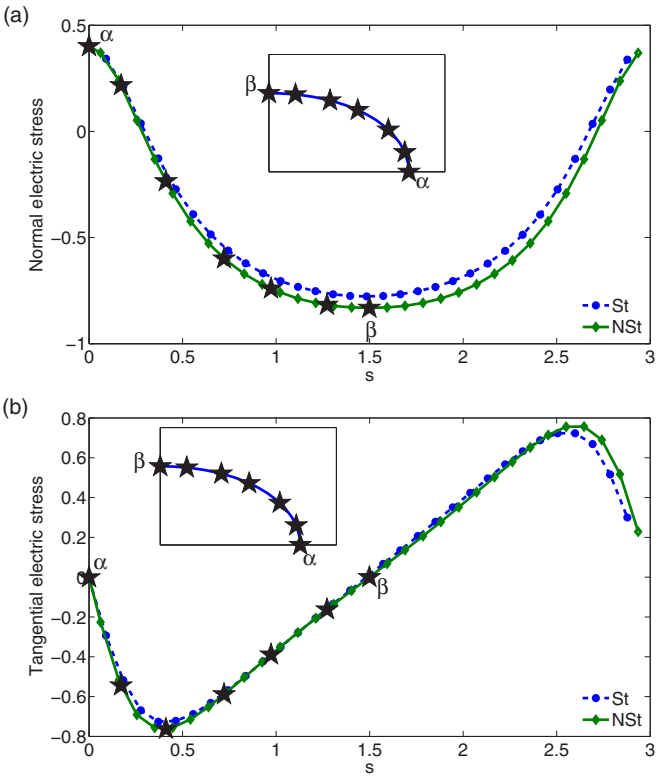

FIG. 6. Normal (a) and tangential (b) electric stresses for Fig. 4(c) (oblate drop). $Ca_E = 0.253$, $Oh = 0.459$ (solid) and $Oh \to \infty$ (dashed, limit of creeping flow). In the legend, *St* denotes Stokes, and *NSt* denotes Navier-Stokes.

difference in tangential stress between Stokes and Navier-Stokes flows (an observation that is also valid for $D < 0$), there is a significant difference in the normal electric stress around the pole. In the presence of inertia ($Oh = 0.1836$), the greater electric pressure produces larger drop deformation. Figure 6 shows the normal and tangential electric stresses for Fig. 4(c) (oblate drop with $D < 0$), as a function of arc length s. The normal electric stress changes sign along the drop interface, being positive at the equator and strongly negative at the pole. Positive electric pressure at the equator explains the elongation of the drop in the direction perpendicular to the electric field.

Several other combinations of $(\sigma_r, \varepsilon_r)$ from Lac and Homsy [7] are used in our simulations to represent different regions in the (R, Q) diagram (Fig. 2 in Lac and Homsy [7]). Figure 7(a) shows a prolate "A" drop (counterclockwise circulation) with $(\sigma_r, \varepsilon_r) = (0.1, 0.04)$. Figure 7(b) shows a prolate "B" drop (clockwise circulation) with $(\sigma_r, \varepsilon_r) = (0.01, 0.1)$. Figure 7(c) shows an oblate drop (clockwise circulation) with $(\sigma_r, \varepsilon_r) = (2, 20)$. For the prolate drops, the Ohnesorge numbers are 0.459, 0.6426, respectively, and $Ca_E = 15$. For the oblate drop, we set $Oh = 0.6426$ and $Ca_E = 0.27$.

Combining Figs. 4 and 7, we observe that the inertia effects on the drop deformation are highly correlated with the direction of the electric stress on the drop interface: Larger drop deformation in the presence of inertia is found when the normal electric stress points outward, while inertia reduces drop deformation when the normal electric stress points inward. Figure 8 shows the distribution of the normal and tangential

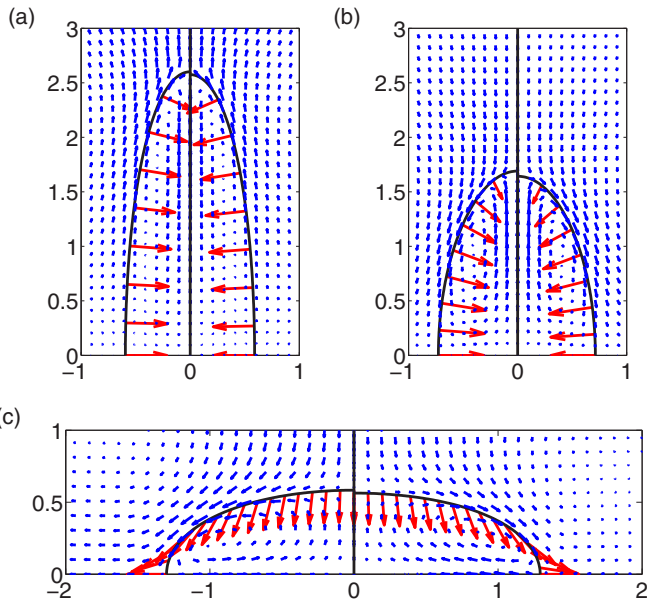

FIG. 7. Comparison between creeping flow (left panel) and Navier-Stokes flow (right panel) for steady-state shape of upper half of drop. (a) Prolate "A": $\sigma_r = 0.1$, $\varepsilon_r = 0.04$; the electric capillary and Ohnesorge numbers are $Ca_E = 15$, $Oh = 0.459$. (b) Prolate "B": $\sigma_r = 0.01$, $\varepsilon_r = 0.1$; the electric capillary and Ohnesorge numbers are $Ca_E = 15$, $Oh = 0.6426$. (c) Oblate: $\sigma_r = 2$, $\varepsilon_r = 20$; the electric capillary and Ohnesorge numbers are $Ca_E = 0.27$, $Oh = 0.6426$. The red arrows represent the electric force acting on the drop interface.

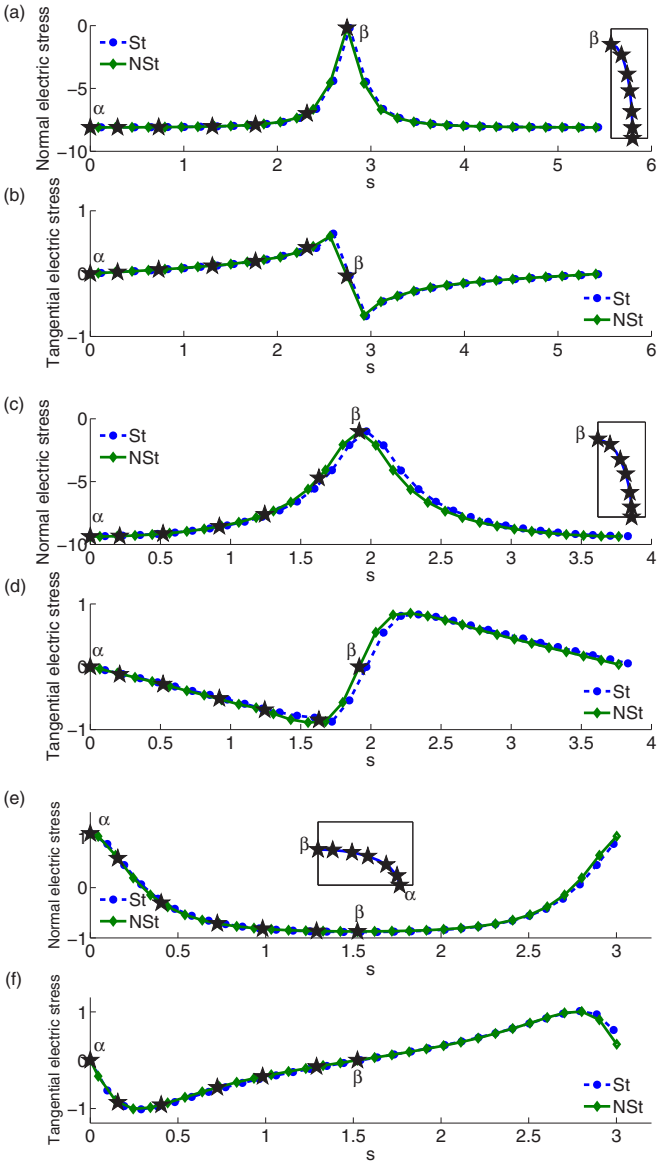

FIG. 8. Electric stresses for drop deformations shown in fig. 7. (a)-(b): $\sigma_r = 0.1$, $\varepsilon_r = 0.04$,$\mathrm{Ca}_E = 15$, $\mathrm{Oh} = 0.459$. (c)-(d): $\sigma_r = 0.01$, $\varepsilon_r = 0.1$,$\mathrm{Ca}_E = 15$, $\mathrm{Oh} = 0.6426$. (e)-(f): $\sigma_r = 2$, $\varepsilon_r = 20$,$\mathrm{Ca}_E = 0.27$, $\mathrm{Oh} = 0.6426$.

electric stresses along the fluid interface for the three cases in Fig. 7. As the drop deformation is similar between Stokes and Navier-Stokes flows for all three cases, the electric stresses are similar in all three cases as expected.

C. Drop deformation above critical capillary number

Under a strong electric field, the steady equilibrium drop shape often ceases to exist for electric capillary number $\mathrm{Ca}_E > \mathrm{Ca}_{E,\mathrm{cr}}$, and the drop becomes unstable and breaks up through one of two modes: pinch-off or tip-streaming. In the pinch-off mode, a single drop deforms into two bulbous ends connected by a thin thread, which eventually pinches as the drop breaks into multiple daughter drops. In the tip-streaming mode, the formation of a conical end (also known as Taylor cone) precedes the emission of fluid jets through the pointed ends.

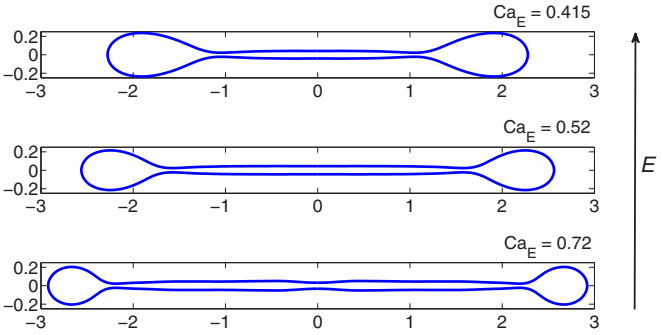

FIG. 9. Onset of drop pinch-off for the oblate shape. Conductivity and permittivity ratios are $\sigma_r = 0.1$, $\varepsilon_r = 2$. $\mathrm{Oh} = 0.6426$ and $\mathrm{Ca}_E = 0.415,\ 0.52,\ 0.72$ at times $T = 5.78,\ 4.24,\ 2.98$, from top to bottom. The arrow represents the direction of the electric field.

Of the two modes, tip-streaming in electrohydrodynamics has been studied extensively, in a wide range of cases, such as with perfect dielectric [8,17,30], electrolytic solutions [31], in the presence of surfactants [32], in non-Newtonian fluids [9], and between liquid-gas interfaces [20]. In the present case of a leaky dielectric drop immersed in another leaky dielectric fluid, the pinch-off mechanism is typically observed [9,32]. However, exceptions have been reported, such as in the case of prolate drops with clockwise circulation [7].

In this section, we investigate the inertia effect on drop electrohydrodynamics when $\mathrm{Ca}_E > \mathrm{Ca}_{E,\mathrm{cr}}$. We focus on oblate deformations and use the same ratios of conductivities and permittivities as in Sec. IV B.

The critical capillary number for an oblate drop with $\sigma_r = 0.1$ and $\varepsilon_r = 2$ has been reported in the range $\mathrm{Ca}_{E,\mathrm{cr}} \approx 0.297$–$0.304$ [7,26]. For Ca_E slightly above the critical value, the drop deforms into a dumbbell shape, pinching off at its center and splitting into two smaller droplets [7,26]. Here we focus on drop dynamics at Ca_E significantly greater than the critical value. Figure 9 shows the oblate drop deformations at various values of $\mathrm{Ca}_E > \mathrm{Ca}_{E,\mathrm{cr}}$. Our simulation results suggest that the drop becomes more elongated as Ca_E increases. At $\mathrm{Ca}_E = 0.415$, the pinch-off now occurs near the end points, suggesting that the drop now breaks into three smaller droplets. As Ca_E is increased to 0.52, we note an indentation at the center of the drop (magnification in Fig. 10). The magnitude of the indentation becomes more pronounced as Ca_E increases. For $\mathrm{Ca}_E = 0.72$, we observe the inertia effects on the drop dynamics (Fig. 11): While the center of the drop remains smooth in creeping flow, inertia effects cause severe indentation at the center. As a result of the inertia-induced indentation at the center of the drop, we suspect that more daughter drops may be found for the drop with inertia than without.

The drop shapes in Fig. 11 are shown at the onset of drop pinch-off. Focusing on the onset of drop pinch-off, we find that inertia effects give rise to an earlier onset of drop pinch-off. For $\mathrm{Ca}_E = 0.52$, the drop begins to pinch-off at $T = 6.15$ in creeping flow, compared to $T = 4.24$ with inertia. The difference in time is reduced at a higher $\mathrm{Ca}_E = 0.72$: $T = 3.96$ in creeping flow, and $T = 2.98$ with inertia. The observation that inertia effects expedite the onset of pinch-off

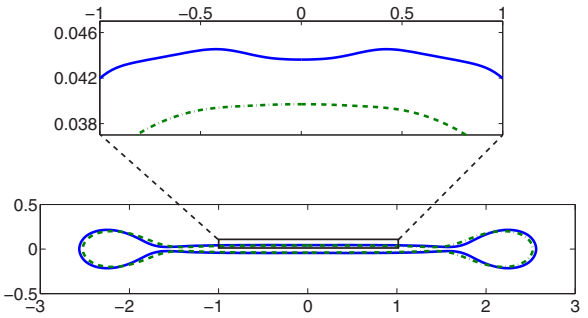

FIG. 10. Comparison of onset of drop pinch-off between the Stokes (dashed) and Navier-Stokes (solid) simulations with Oh = 0.6426 and $Ca_E = 0.52$. The inset shows the detailed drop shape at the center. This pinch-off dynamic is more apparent at higher electric capillary number, as shown in Fig. 11.

is consistent with the inertia effects on drop deformation for Ca_E below critical: drops in Navier-Stokes flow reach their steady equilibrium shape more rapidly than in creeping flow.

Figure 12 shows the flow field around the drop shapes in Fig. 9. We observe that the flow is strongest near the neck, moving in the direction toward pinching the neck. Away from the neck, the fluid flow is relatively quiescent. To develop a better understanding of the pinch-off drop dynamics, we analyze the electric stresses as we did in Sec. IV B. Figure 13 shows the normal and tangential Maxwell stresses for the case with $Ca_E = 0.72$ in Fig. 11. In Fig. 13(a), the symbols correspond to various positions on the drop's interface (inset), with α at the equator and β at the pole.

The normal electric stress sheds light on the formation of the indentation at the drop center, which is also a site for drop pinch-off at higher Ca_E. From Fig. 13(a), we observe the minima in normal electric stress correspond to possible pinch-off sites on the drop interface, including one at location β (see Fig. 13). They also represent regions of greatest negative electric pressure. By comparison, for viscous drops in Stokes flow, the minima at β does not appear and the possible pinch-off sites are near the bulbous end of the drop. We therefore speculate that for an oblate drop ($D < 0$), the normal electric

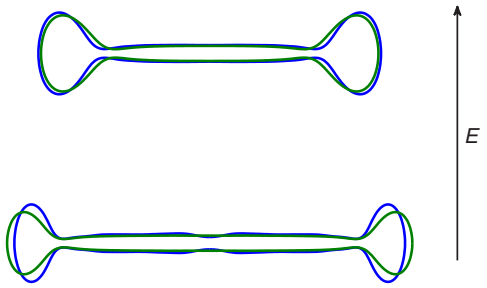

FIG. 11. Comparison of extreme drop deformation, between the Stokes (dashed) and Navier-Stokes (solid) simulations. Oh = 0.6426, $Ca_E = 0.52$, (top) and $Ca_E = 0.72$ (bottom). For $Ca_E = 0.52, T = 6.15$ (Stokes) and $T = 4.24$ (Navier-Stokes). For $Ca_E = 0.72$, $T = 3.96$ (Stokes) and $T = 2.98$ (Navier-Stokes). The arrow represents the direction of the electric field.

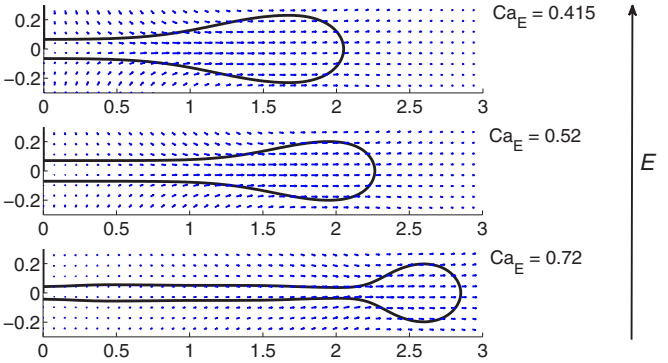

FIG. 12. Flow field at the onset of drop pinch-off for the oblate shape. Conductivity and permittivity ratios are $\sigma_r = 0.1$, $\varepsilon_r = 2$. Oh = 0.6426 and $Ca_E = 0.415, 0.52, 0.72$ at times $T = 5.37, 3.9, 2.93$, from top to bottom. The arrow represents the direction of the electric field.

stress would be a useful tool to study the breakup dynamics of a viscous drop.

V. CONCLUSION

In this study, we numerically investigated the electrohydrodynamics of a viscous drop under a uniform DC electric field. We focus on the drop deformation in relation to the

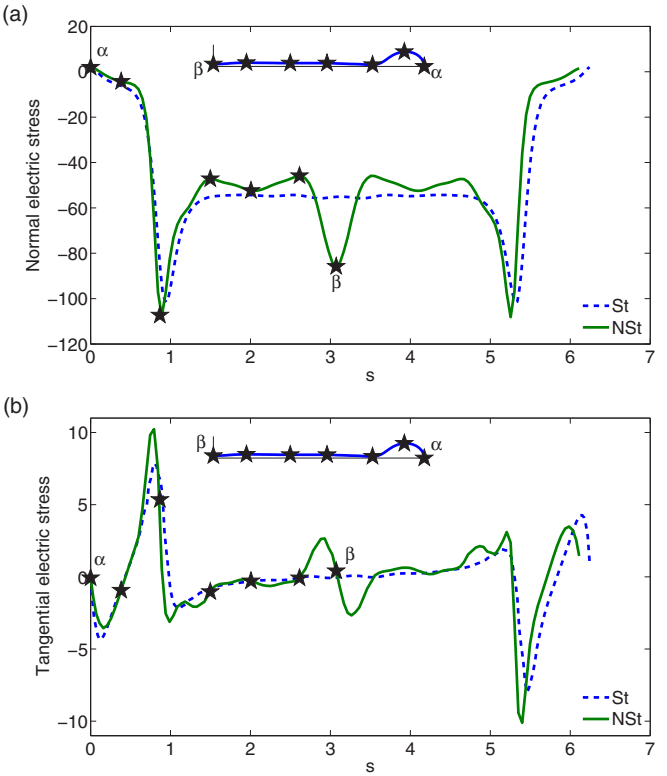

FIG. 13. Normal (a) and tangential (b) electric stresses for the oblate deformation with $Ca_E = 0.72$. Other parameters are Oh = 0.6426 (solid) and Oh $\to \infty$ (dashed, limit of creeping flow). The symbols in (a) show the value of the stress at various positions on the drop interface (inset).

spatial distribution of forces and stresses on the interface of a leaky dielectric viscous drop under a DC electric field. The present results also attempt to uncover the principal features that differentiate the electrohydrodynamics of viscous drops in Navier-Stokes flows from those in Stokes flow. In particular we elucidate the dependence of the electrohydrodynamics of a viscous drop on both the electric capillary number Ca_E and Ohnesorge number Oh.

For most combinations of $(\sigma_r, \varepsilon_r)$, a critical electric field strength exists such that a steady equilibrium drop is possible only for $\mathrm{Ca}_E < \mathrm{Ca}_{E,\mathrm{cr}}$. For some combinations, however, a steady equilibrium drop is possible even under an extremely large electric field [$\mathrm{Ca}_E \gg 1$, such as Fig. 7(a)]. In Sec. IV B we reported results from a numerical investigation of the inertia effects on the steady equilibrium drop shape for prolate "A," prolate "B," and oblate drops. Previous studies reported that inertia leads to higher prolate "A" deformations compared to creeping flow, consistent with our numerical results. We also found that the inertia effects on the equilibrium drop deformation number D are highly correlated with the direction of electric stresses along the drop interface: the magnitude of D increases due to inertia when the electric stresses point outward, while the drop deformation is decreased by inertia when the electric stresses point inward.

When the electric capillary number is above the critical value ($\mathrm{Ca}_E > \mathrm{Ca}_{E,\mathrm{cr}}$), we observed several distinct features. Firstly, no steady equilibrium drop shape exists and the type and mode of the subsequent drop breakup are dependent on the electric capillary number, Ca_E. As Ca_E increases, the drop becomes more elongated prior to breakup, which often happens as the drop pinches off at the bulbous ends. Increasing Ca_E resulted in two (Stokes flow) or more (Navier-Stokes flow) droplets being formed. We showed that in the presence of inertia, small indentations are found at the center of the elongated drop. The indentations became more pronounced with Ca_E, yielding to pinch-offs at the drop center (in addition to those at the bulbous ends). Secondly, inertia led to faster dynamics than in the case of Stokes flow. This observation holds regardless of the electric capillary number.

Finally, we presented results for the Maxwell stresses for oblate drop deformations above critical Ca_E. We found that in the case of Navier-Stokes flows, large electric pressure gradients along the drop interface positively correlate with sites of pinch-offs. To our knowledge, such a connection has not been reported previously for oblate drops. Moreover, our results suggest that drop breakup through pinch-off could be predicted from analyzing the electric stresses along the drop interface.

In our leaky dielectric formulation we neglected the effects of surface charge transport, which is found to be important for a slightly deformed oblate viscous drop in an electric field [33]. In particular, the surface charge relaxation is found to reduce the oblate deformation at high electric field strength [33], while in the prolate case the charge transport may lead to jet formation near the poles [31]. In an ongoing work we are investigating how charge convection may affect the dynamics for both oblate and prolate drops, and how these drop dynamics in leaky dielectric formulation may differ from those in electrokinetic framework.

ACKNOWLEDGMENTS

Y.-N. Young acknowledges support from NSF under Grants No. DMS-1222550 and No. DMS-1412789. M.-C. Lai acknowledges partial support from the National Science Council of Taiwan under research Grant No. NSC-101-2115-M-009-014-MY3 and NCTS. A. Layton acknowledges support from NSF under Grant No. DMS-126395.

[1] Geoffrey Taylor, Studies in electrohydrodynamics. I. The circulation produced in a drop by electric field, Proc. R. Soc. Lond. A **291**, 159 (1966).

[2] J. R. Melcher and G. I. Taylor, Electrohydrodynamics: A review of the role of interfacial shear stresses, Ann. Rev. Fluid Mech. **1**, 111 (1969).

[3] O. O. Ajayi, A note on Taylor's electrohydrodynamic theory, Proc. R. Soc. Lond. A **364**, 499 (1978).

[4] N. Bentenitis and S. Krause, Droplet deformation in DC electric fields: The extended leaky dielectric model, Langmuir **21**, 6194 (2005).

[5] J. Zhang, J. D. Zahn, and H. Lin, Transient solution for droplet deformation under electric fields, Phys. Rev. E **87**, 043008 (2013).

[6] N. Dubash and A. J. Mestel, Behavior of a conducting drop in a highly viscous fluid less conducting than that of the ambient fluid, J. Fluid Mech. **581**, 469 (2007).

[7] E. Lac and G. M. Homsy, Axisymmetric deformation and stability of a viscous drop in a steady electric field, J. Fluid Mech. **590**, 239 (2007).

[8] G. Supeene, C. R. Koch, and S. Bhattacharjee, Deformation of a droplet in an electric field: Nonlinear transient response in perfect and leaky dielectric media, J. Colloid Int. Sci. **318**, 463 (2008).

[9] J.-W. Ha and S.-M. Yang, Deformation and breakup of Newtonian and non-Newtonian conducting drops in an electric field, J. Fluid Mech. **405**, 131 (2000).

[10] J. S. Eow, M. Ghadiri, and A. Sharif, Deformation and breakup of aqueous drops in dielectric liquids in high electric fields, J. Electrostat. **51-52**, 463 (2001).

[11] J. S. Eow and M. Ghadiri, Motion, deformation and breakup of aqueous drops in oils under high electric field strengths, Chem. Eng. Proc. **42**, 259 (2003).

[12] P. F. Salipante and P. M. Vlahovska, Electrohydrodynamics of drops in strong uniform dc electrid fields, Phys. Fluids **22**, 112110 (2010).

[13] R. B. Karyappa, S. D. Deshmukh, and R. M. Thaokar, Breakup of a conducting drop in a uniform electric field, J. Fluid Mech. **754**, 550 (2014).

[14] A. Beroual, Dynamics of water droplets immersed in dielectric liquids submitted to electric stress, IEEE Trans. Dielec. Elect. Insul. **22**, 359 (2015).

[15] H. Nganguia, Y.-N. Young, P. M. Vlahovska, J. Bławzdziewcz, J. Zhang, and H. Lin, Equilibrium electro-deformation of

a surfactant-laden viscous drop, Phys. Fluids **25**, 092106 (2013).

[16] J. Q. Feng and T. C. Scott, A computational analysis of electrohydrodynamics of a leaky dielectric drop in an electric field, J. Fluid Mech. **311**, 289 (1996).

[17] J. D. Sherwood, Breakup of fluid droplets in electric and magnetic fields, J. Fluid Mech. **188**, 133 (1998).

[18] N. Dubash and A. J. Mestel, Breakup behavior of a conducting drop suspended in a viscous fluid subject to an electric field, Phys. Fluids **19**, 072101 (2007).

[19] H. Paknemat, A. R. Pishevar, and P. Pournaderi, Numerical simulations of drop deformations and breakup modes caused by direct current electric fields, Phys. Fluids **24**, 102101 (2012).

[20] R. T. Collins, K. Sambath, M. T. Harris, and O. A. Basaran, Universal scaling laws for the disintegration of electrified drops, Proc. Natl. Acad. Sci. USA **110**, 4905 (2013).

[21] J. A. Lanauze, L. M. Walker, and A. S. Khair, The influence of inertia and charge relaxation on electrohydrodynamic drop deformation, Phys. Fluids. **25**, 112101 (2013).

[22] O. Schnitzer and E. Yariv, The Taylor-Melcher leaky dielectric model as a macroscale electrokinetic description, J. Fluid Mech. **773**, 1 (2015).

[23] L. C. McConnell, M. J. Miksis, and P. M. Vlahovska, Vesicle electrohydrodynamics in DC electric fields, IMA J. Appl. Math. **78**, 797 (2013).

[24] J. Q. Feng, Electrohydrodynamic behavior of a drop subjected to a steady uniform electric field at finite electric Reynolds number, Proc. Math. Phys. Eng. Sci. **455**, 2245 (1999).

[25] M.-C. Lai, C.-Y. Huang, and Y.-M. Huang, Simulating the axisymmetric interfacial flows with insoluble surfactant by immersed boundary method, Int. J. Numer. Anal. Modeling **8**, 105 (2011).

[26] H. Nganguia, Y.-N. Young, A. T. Layton, W.-F. Hu, and M.-C. Lai, An immersed interface method for axisymmetric electrohydrodynamic simulations in stokes flow, Comm. in Comput. Phys. **18**, 429 (2015).

[27] W.-F. Hu, M.-C. Lai, and Y.-N. Young, A hybrid immersed boundary and immersed interface method for electrohydrodynamic simulations, J. Comput. Phys. **282**, 47 (2015).

[28] T. Beale and A. T. Layton, A velocity decomposition approach for moving interfaces in viscous fluids, J. Comput. Phys. **228**, 3358 (2009).

[29] Y. Li, I. Sgouralis, and A. T. Layton, Computing viscous flow in an elastic tube, Numer. Math. Theor. Meth. Appl. **7**, 555 (2014).

[30] S. D. Deshmukh and R. M. Thaokar, Deformation, breakup and motion of a perfect dielectric drop in a quadrupole electric field, Phys. Fluids **24**, 032105 (2012).

[31] R. Pillai, J. D. Berry, D. J. E. Harvie, and M. R. Davidson, Electrolytic drops in an electric field: A numerical study of drop deformation and breakup, Phys. Rev. E **92**, 013007 (2015).

[32] J.-W. Ha and S.-M. Yang, Effect of nonionic surfactant on the deformation and breakup of a drop in an electric field, J. Colloid Int. Sci. **206**, 195 (1998).

[33] J. A. Lanauze, L. M. Walker, and A. S. Khair, Nonlinear electrohydrodynamics of slightly deformed oblate drops, J. Fluid Mech. **774**, 245 (2015).